crystals

MDPI

Article

Analysis of Human Kidney Stones Using Advanced Characterization Techniques

Jelena Brdarić Kosanović [1], Kristijan Živković [1], Vatroslav Šerić [2], Berislav Marković [3], Imre Szenti [4], Ákos Kukovecz [4], Nives Matijaković Mlinarić [5] and Anamarija Stanković [1,*]

[1] Department of Chemistry, University of Osijek, Cara Hadrijana 8/A, 31000 Osijek, Croatia; jbrdaric@kemija.unios.hr (J.B.K.); zivkovi.kristijan@gmail.com (K.Ž.)
[2] Clinical Institute for Laboratory Diagnostics, University Hospital Osijek, 31000 Osijek, Croatia; vatroslav.seric.os@gmail.com
[3] Faculty of Dental Medicine and Health Osijek, Crkvena 21, 31000 Osijek, Croatia; bmarkovic@fdmz.hr
[4] Department of Applied and Environmental Chemistry, University of Szeged, Rerich Béla tér 1, H-6720 Szeged, Hungary; szentiimre@gmail.com (I.S.); kakos@chem.u-szeged.hu (Á.K.)
[5] Ruđer Bošković Institute, Bijenička pregledali smo sta 54, 10000 Zagreb, Croatia; nives.matijakovic@irb.hr
[*] Correspondence: ster.anamarija@gmail.com or astankovic@kemija.unios.hr; Tel.: +385-31399959

Abstract: A comprehensive analysis of kidney stones is essential for the future treatment of patients. Almost all of the methods available for kidney stone analysis were used in this study. The chemical analysis included powder X-ray diffraction (PXRD), Fourier transform infrared spectroscopy (FTIR), and thermogravimetric analysis (TGA-DSC). Following the chemical analysis, a detailed morphological analysis was carried out using stereoscopic microscopy, scanning electron microscopy (SEM-EDX), and micro-computed tomography (micro-CT). These investigations showed that the sixteen kidney stones analyzed in detail had a heterogeneous mineralogical structure, consisting of at least two different minerals. Kidney stones consist mainly of calcium oxalate (whewellite or weddellite) but also contain significant amounts of phosphate (mainly apatite and struvite). A thorough analysis of kidney stones can determine the cause of their formation and investigate possible treatments.

Keywords: kidney stones; calcium oxalate; phosphate; chemical analysis

check for updates

Academic Editor: José Gavira

Received: 6 December 2024
Revised: 22 December 2024
Accepted: 23 December 2024
Published: 25 December 2024

Citation: Brdarić Kosanović, J.; Živković, K.; Šerić, V.; Marković, B.; Szenti, I.; Kukovecz, Á.; Matijaković Mlinarić, N.; Stanković, A. Analysis of Human Kidney Stones Using Advanced Characterization Techniques. *Crystals* **2025**, *15*, 6. https://doi.org/10.3390/cryst15010006

Copyright: © 2024 by the authors. Licensee MDPI, Basel, Switzerland. This article is an open access article distributed under the terms and conditions of the Creative Commons Attribution (CC BY) license (https://creativecommons.org/licenses/by/4.0/).

1. Introduction

Biomineralization is a fundamental biological process observed in both animals and humans, crucial for the development and maintenance of hard tissues such as bones, cartilage, and teeth [1,2]. Under normal physiological conditions, mineralization supports tissue formation and repair. However, this process can also occur pathologically in soft tissues, leading to a variety of diseases. Pathological mineralization involves the abnormal deposition of minerals, including calcium phosphates [3,4], calcium carbonates [5], and calcium oxalates [6,7], in soft tissues. Although various molecular mechanisms explaining pathological calcification have been proposed, the exact causes and mechanisms of mineral formation in the affected tissues remain only partially understood [8–11]. Traditionally, much of the research in this area has focused on indirect studies of these minerals, often overlooking their in vivo characteristics, which can be captured better through direct material characterization techniques like electron microscopy [3] and spectroscopy [12].

Among the most recognized forms of pathological mineralization is kidney stone disease (nephrolithiasis) [13], a widespread condition affecting millions globally. This disease is characterized by the formation of kidney stones, which are often recurrent after treatment [14] and have been linked to a variety of systemic diseases, such as hyperparathyroidism [14], obesity [15], diabetes [16], metabolic syndrome [17], and cardiovascular complications [18,19]. In most cases, kidney stones arise from metabolic disorders that lead to imbalances in urinary composition, resulting in the supersaturation of certain minerals [14,20].

The composition of kidney stones has been studied extensively, revealing a variety of mineral phases [21,22]. While the majority of kidney stones primarily comprise calcium oxalate, often in the forms of whewellite or weddellite [23], up to 50% of stones also contain calcium phosphate [21,24]. Other less common types include magnesium ammonium phosphate, urate, and cystine stones [24]. The formation of these stones is often associated with conditions such as hyperoxaluria, hypercalciuria, and a low urinary pH, all of which promote mineral crystallization through supersaturation processes [21,22].

Given the heterogeneous nature of kidney stones, the precise identification of their elemental and mineral composition is critical for determining the most effective treatment strategies. This task has been made possible through advancements in material characterization techniques. Modern diagnostic workflows now routinely employ methods such as Fourier transform infrared spectroscopy (FTIR), powder X-ray diffraction (PXRD), thermogravimetric analysis (TGA-DSC), scanning electron microscopy (SEM/EDX), and micro-computed tomography (micro-CT) analysis to provide detailed insights into the chemical and structural properties of kidney stones.

In this study, we aim to advance the characterization of the crystalline phases present in kidney stones using a combination of PXRD, FTIR, SEM/EDX, and micro-CT. By examining 16 kidney stones collected from surgeries performed at the University Hospital Center Osijek, we provide a comprehensive guide on the most common crystalline phases and demonstrate how these analytical techniques enable their accurate identification.

2. Materials and Methods

2.1. Materials

Sixteen kidney stone samples were collected from University Hospital Center Osijek (according to FURS (flexible ureterorenoscopy)), of which eight stones belonged to the female population (F1-8) and eight to the male population (M1-8) (Table 1). The original stones (in the kidneys) were almost always larger because they are broken into smaller pieces during the FURS procedure. The analysis shows (Table 1) that M1, M3, M5, M6, and F6 are predominantly oxalate stones. F4, F5, and F8 are mixed stones (predominantly oxalate stones with a small amount of phosphate), while F1, F2, F3, M2, M4, and M7 predominantly contain calcium phosphates. Sample F7 consisted of calcium oxalate (whewellite) and uric acid, while M8 consisted mainly of cystine and phosphate (struvite). The kidney stone samples are presented with the patient's year of birth and their mineral composition in Supplementary Table S1.

Table 1. Kidney stone sample types classified into two groups according to mineral composition.

Kidney Stone Group	Samples	Kidney Stone Type (Mineral Name)
Calcium kidney stones	M1, M3, M5, M6, F6	Mostly calcium oxalate (whewellite (*w*), weddellite (*wd*))
	F4, F5, F8	Mixed calcium oxalate (whewellite (*w*), weddellite (*wd*), + calcium phosphate hydroxyapatite (*a*))

Table 1. *Cont.*

Kidney Stone Group	Samples	Kidney Stone Type (Mineral Name)
Calcium kidney stones	F1, F2, F3, M2, M4, M7	Mostly calcium phosphate (hydroxyapatite (*a*) and struvite (*s*)) + some weddellite (*wd*) and a very small amount of whewellite (*w*))
Non-calcium kidney stones	F7	Mixed calcium oxalate (*w*) + uric acid (*u*)
	M8	Mixed cystine (*c*) + phosphate struvite (*s*)

2.2. Methods

The kidney stone samples were characterized using stereoscopic microscopy (SM), simultaneous thermogravimetric analysis and differential scanning calorimetry (TGA/DSC), Fourier transform infrared spectroscopy (FTIR), scanning electron microscopy with energy-dispersive X-ray spectroscopy (SEM/EDX), powder X-ray diffraction (PXRD), and micro-computed tomography (micro-CT imaging).

Visual identification of the oxalates and determination of their morphological properties were performed using stereoscopic microscopy (with an Orthoplan photographic microscope, E. Leitz, Leica, Wetzlar, Germany) and SEM with a Thermo Fisher Scientific Apreo C scanning electron microscope (Thermo Fisher Scientific, Waltham, MA, USA). Energy-dispersive X-ray spectroscopy and scanning electron microscopy (SEM/EDX) were used to determine the samples' elemental composition. The microscope was operated at a 40 mA current and a 20 kV acceleration voltage. The IR spectra were recorded on a Shimadzu FTIR 8400S (Shimadzu Corp., Kyoto, Japan) spectrometer in a wavenumber range from 400 to 4000 cm^{-1} (resolution: 4 cm^{-1}). IR Solution 1.30 software was used to record the spectra and process the data. The qualitative and quantitative analyses were carried out using the Urea Stone library with the DRIFT Shimadzu database. The PXRD data were collected using a PANalytical Aeris diffractometer (Malvern PANalytical, Malvern, UK) using Cu Kα radiation (40 kV, 15 mA, with a step size of 0.02 and a 1° divergence slit) in the range of 10–60° 2Θ. The detected phases were identified using the Crystallography Open Database (COD), and qualification and quantification of the phases were undertaken with Rietveld refinement using the HighScorePlus software 3.0.

The TGA/DSC analysis was conducted on a Mettler Toledo System 1 (Mettler Toledo, Columbus, OH, USA). The samples were tested in an oxygen atmosphere at a gas flow rate of 200 $\text{cm}^3\ \text{min}^{-1}$ and a heating rate of 5 °C min^{-1} in a temperature range of 30 to 900 °C. The results were processed using STARe Software 10.0. Micro-CT imaging was performed using a Tescan UniTOM XL cone-beam scanner (Tescan, Czech Republic) at the University of Szeged, Hungary, with X-ray source settings of a 120 kV source voltage and a 20 W tube power. Each sample was measured in micro-focus mode using an XRD4343_1920x1896 ~3.5 µm voxel resolution. The acquired images were reconstructed using the volumetric Panthera Reconstruction Software 1.4.4.20. (Tescan, Czech Republic). During this reconstruction, typically occurring artifacts, such as ring artifacts and beam-hardening artifacts, were corrected.

3. Results and Discussion

As described in the literature, kidney stones contain $\leq$90% mineral compounds and $\geq$10% organic compounds. These mineral compounds are the subject of this study [21–24]. Kidney stones can generally be categorized into stones that consist of calcium minerals, such as calcium oxalate (CaOx—whewellite and weddellite) and calcium phosphate (apatite, struvite, and brushite), and stones that do not contain calcium (e.g., uric acid, cystine, protein, and drug stones) [25]. The majority of kidney stones contain calcium oxalate

(60–75%) or calcium phosphate (15–20%). Other less common stone compositions are uric acid and cystine [26–28]. In this article, we will categorize the results into the two broad categories we have just mentioned: calcium kidney stones and non-calcium kidney stones [29–33].

3.1. Calcium Stones

3.1.1. Calcium Oxalate Kidney Stones

Oxalates are salts of a strong dicarboxylic acid ($C_2O_4H_2$) which are formed in the body through a combination of food sources and endogenous synthesis from precursors such as ascorbate and/or amino acids. Increased absorption of oxalate from food, as well as increased endogenous production of oxalate, can cause the formation of calcium oxalate (CaOx) stones [34].

The main forms of calcium oxalate are whewellite (monohydrate, $CaC_2O_4 \times H_2O$, *w*) and weddellite (dihydrate, $CaC_2O_4 \times 2H_2O$, *wd*), which occur extensively in fossil rocks, microorganisms, plants, and human urinary calculi. Whewellite has a monoclinic crystal form, while weddellite has a tetragonal crystal form, although both can crystallize in a variety of forms, such as tetragonal bipyramids, prisms, tablets, and needles [35]. Weddellite is an unstable modification and changes to whewellite after some time, so a mixture of weddellite and whewellite is quite common [36].

Analysis of Kidney Stones M1, M3, M5, M6, and F6

As in the IR spectra of the other samples, there is a band that corresponds to symmetrical and asymmetrical OH^- stretching in the water molecule at 3000–3600 cm^{-1}. Two sharp peaks at 1316 and 700 cm^{-1} and two weaker peaks at 661 and 517 cm^{-1} show the presence of oxalate ions. From the available literature [37], it can be concluded that all of the samples in this group (M1, M3, M5, M6, and F6) contain a significant amount of whewellite, as the OH^- stretching at 3000–3600 cm^{-1} occurs in five different bands (Figure 1). The C=O bond stretching band can be seen at about 1700 cm^{-1}. While M1, M5, M6, and F6 contain over 90% whewellite, the composition of sample M3 is more complex. Sample M3 contains both forms of calcium oxalate (*w* and *wd*) but also a smaller proportion of phosphate (a). A more significant difference can be observed near 950 cm^{-1} and 880 cm^{-1}, as sample M3 does not show any significantly pronounced peaks in this region, while a single broad absorption peak appears at around 3530 cm^{-1} in the OH stretching region.

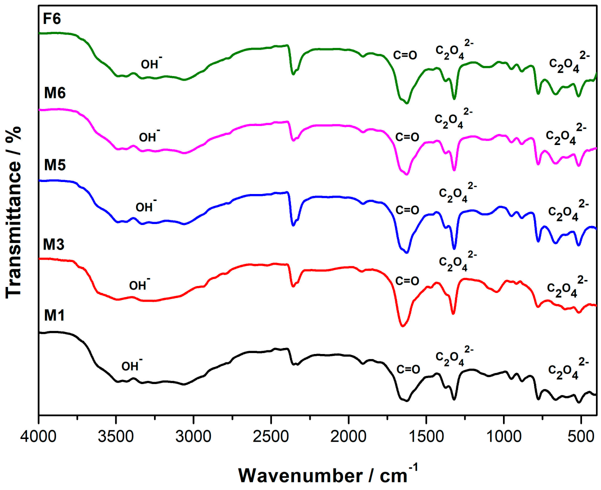

Figure 1. IR spectra of five kidney stone samples: M1, M3, M5, M6, and F6. Data collected using DRIFT technique. Samples (5 mg) were mixed with spectroscopy-grade KBr (100 mg) before analysis. Characteristic bands are labelled at observed wavenumber.

The X-ray diffraction data report (Figure 2) confirms that samples M1, M5, F6, and M6 are almost pure calcium oxalate monohydrate (*w*), with an amount of 90% *w* for sample M1, 98% for F6, and 99% for samples M5 and M6. Sample M3 is mostly composed of calcium oxalate dihydrate (*wd*) (68%), with a lesser amount of *w* (24%) and possibly a small quantity of calcium phosphate *a* (hydroxyapatite, <8%). Calcium oxalate monohydrate was identified according to PDF card number 20-0231, while calcium oxalate dihydrate was identified based on PDF card number 17-541.

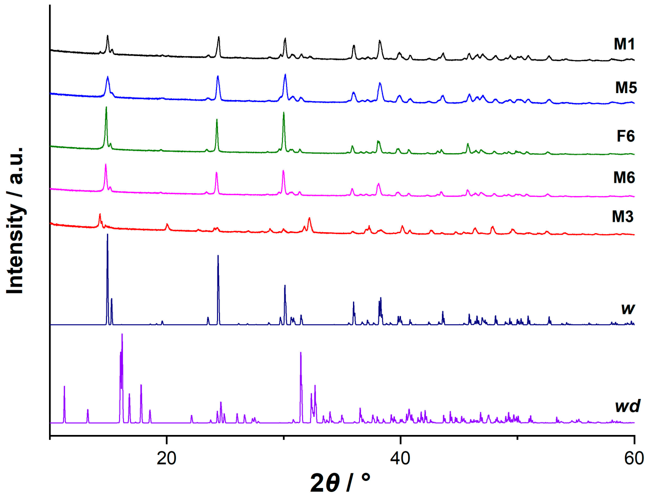

Figure 2. PXRD patterns of five kidney stone samples (M1, M3, M5, M6, and F6) compared to standard data from the Powder Diffraction File (PDF) of whewellite (*w*) and weddellite (*wd*).

The thermogram of sample M1 (mixed whewellite and weddellite) measured in the temperature range from 30 to 900 °C shows the mass loss in three steps (Figure 3). In the first step from 100 to 250 °C, dehydration occurs; the next loss, in the temperature range of 350–500 °C, corresponds to the decomposition of anhydride oxalate and the release of CO; and from 600 to 800 °C, the calcium carbonate decomposes [38]. The remaining weight percent after heating is 40.48%. Thermograms of the other materials are shown in the Supplementary Materials (Figure S1).

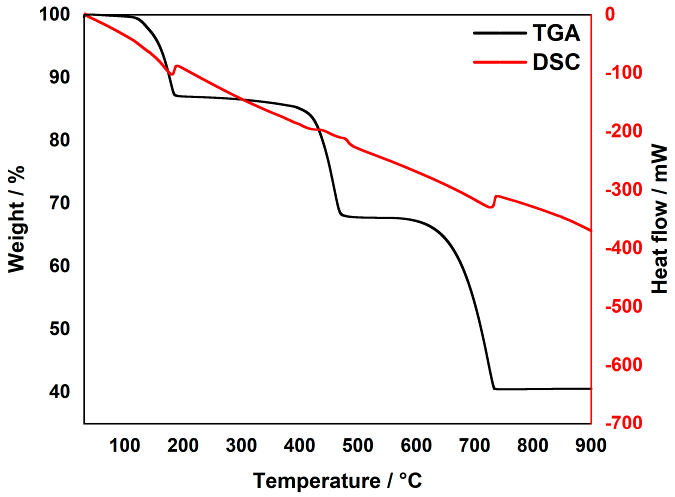

Figure 3. TGA and DSC curves for kidney stone sample M1 in an oxygen atmosphere.

Figure 4 shows stereoscopic microscope images of the stones mostly composed of calcium oxalate (whewellite and weddellite). It is visible that the stones contain light brown papillary skin with white layers, which indicates the presence of calcium oxalates [39].

The approximate sizes of the kidney stone samples are as follows: M1: 8 × 4.5 mm; M3: 4 × 5 mm; M5: 5 × 5.5 mm; M6: 6 × 4.5 mm; and F6: 3 × 3 mm.

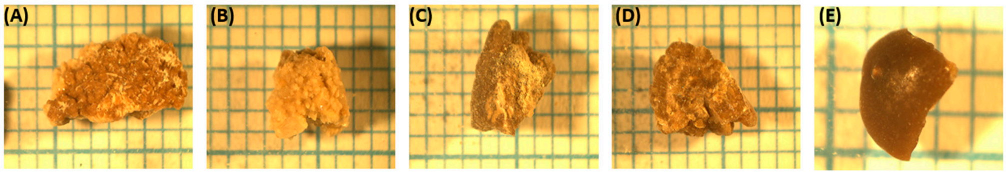

Figure 4. Stereoscopic microscope images of (**A**) M1, (**B**) M3, (**C**) M5, (**D**) M6, and (**E**) F6. Samples are placed on graph paper (1 × 1 mm).

The SEM image of sample M1 (Figure 5A) shows smaller (*w*) and larger (*wd*) crystals. Whewellite crystals have a mesh-like appearance and are small, while weddellite crystals look like layered rectangular blocks [40]. Larger *wd* crystals are present in sample M3, which can be seen in Figure 5B, with a small amount of *w* crystals. The images of samples M5, M6, and M7 (Figure 5C,D) show only small crystals of calcium oxalate monohydrate, which, in some areas, are compacted into large, mesh-like conglomerates. The morphological features of all of the samples in this group are in line with the mineralogical composition revealed using PXRD and IR spectroscopy.

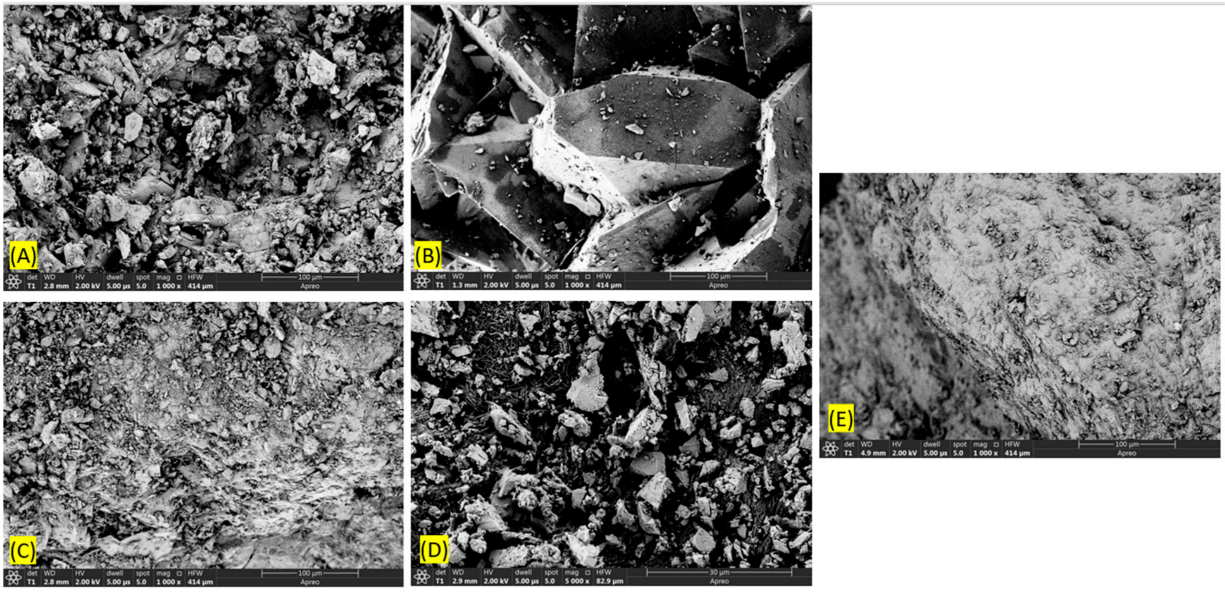

Figure 5. SEM images of (**A**) M1, (**B**) M3, (**C**) M5, (**D**) M6, and (**E**) F6. Magnification at 1000× for M1, M3, M5, and F6 and 5000× (to provide more detail) for M6.

The elemental analysis using EDX confirms the previous conclusion that samples M1, M3, M5, M6, and F6 consist mainly of calcium ions, most likely originating from whewellite (*w*) and weddellite (*wd*). Figure 6 shows the presence of phosphorous (P) in sample M3, which proves the suggestion in the PXRD findings of the presence of a small amount of apatite (EDX findings for the remaining samples are presented in Supplementary Figure S2). Along with the major elements (Ca, C, O, and P), a small amount of various other elements (trace elements) can be observed: K, Mg, Al, and Na. Although the role of trace elements in kidney stone formation is still not fully understood, generally, the presence of small quantities of metallic ions is considered to promote crystallization [41].

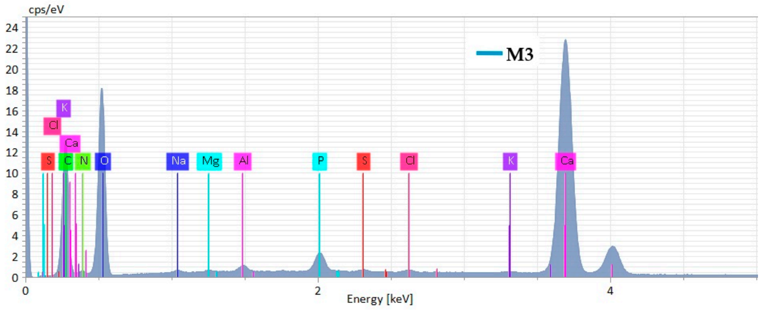

Figure 6. Elemental analysis (EDX) of kidney stone sample M3. The peak height (cps/eV) represents the relative abundance of the detected elements in the sample.

The spatial distribution of the major elements (EDX mapping, Figure 7) in sample M3 shows that along with the uniform presence of calcium, carbon, and oxygen, there are several distinct areas with a high phosphorus content (apatite crystals) [31]. This can be considered definite proof of the mineralogical composition of this sample: 68% *wd*, 24% *w*, and 8% apatite.

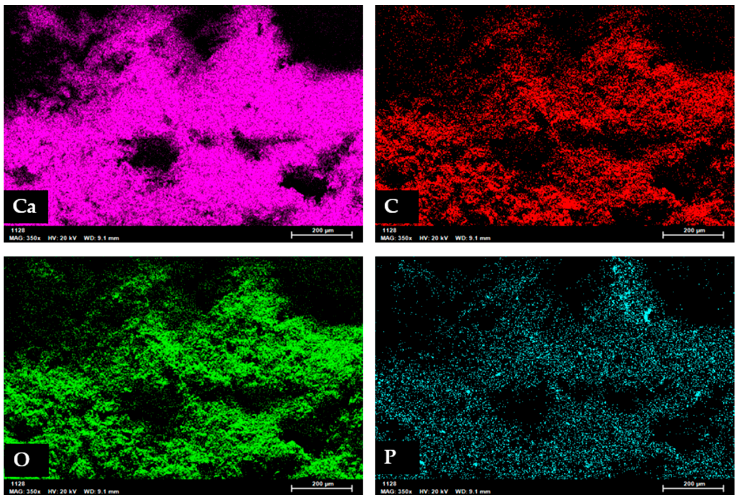

Figure 7. Elemental distribution map of sample M3: Ca, C, O, and P. The intensity of color (brightness) represents the relative amount of a particular element in any given area.

The micro-CT cross-section of sample M5 in Figure 8 shows homogeneous, small, gray, tightly packed calcium oxalate monohydrate crystals and several voids (black spots), most likely due to the proteins that are present during stone crystallization [32].

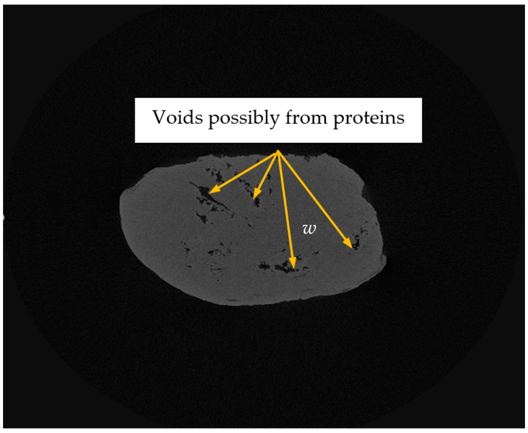

Figure 8. Micro-CT cross-section of kidney stone sample M5 (scan #1358 out of the 1592 collected in total is presented).

Analysis of Kidney Stones F4, F5, and F8

According to the IR spectra shown in Figure 9, the band corresponding to the stretching of the OH^- group can be observed at 3000–3600 cm^{-1}, which is usual for calcium oxalate weddellite. At about 1700 cm^{-1}, the band from C=O bond stretching can be seen, the band from C-O bond stretching is seen at around 1300 cm^{-1}, and the band from C-H bond bending is seen at 500–800 cm^{-1}. The evidence of the presence of calcium phosphate in samples F4 and F5 is the characteristic peak for phosphate ions that can be observed at 900–1200 cm^{-1} [42].

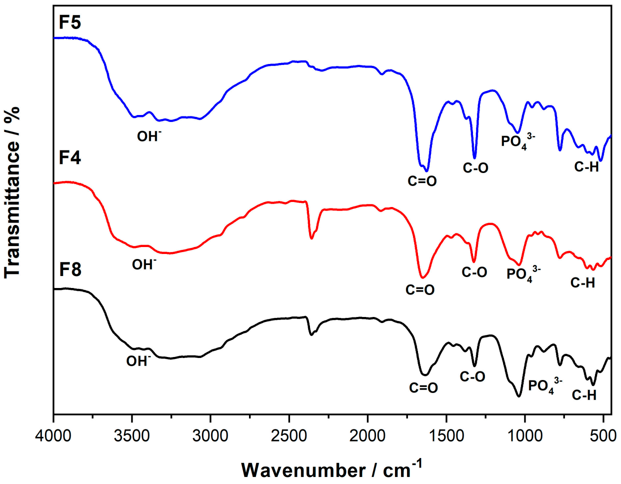

Figure 9. IR spectra of kidney stone samples F8, F4, and F5. Data collected using DRIFT technique. Samples (5 mg) were mixed with spectroscopy-grade KBr (100 mg) before analysis. Characteristic bands are labeled at observed wavenumber.

The X-ray diffraction data generally confirm the mineralogical composition of kidney stone samples F8, F5, and F4 (Figure 10). All of these samples are primarily composed of *wd* and *w*, but all of them show the presence of hydroxyapatite. Sample F8 mostly comprises whewellite (51%), with weddellite (32%) and a small amount of hydroxyapatite (16%) as well. Stone F5 contains 68% whewellite, 19% weddellite, and also a small amount of apatite (12%). The mineral composition of kidney stone F4 is weddellite (46%), hydroxyapatite [43] (34%), and a smaller amount of whewellite (20%).

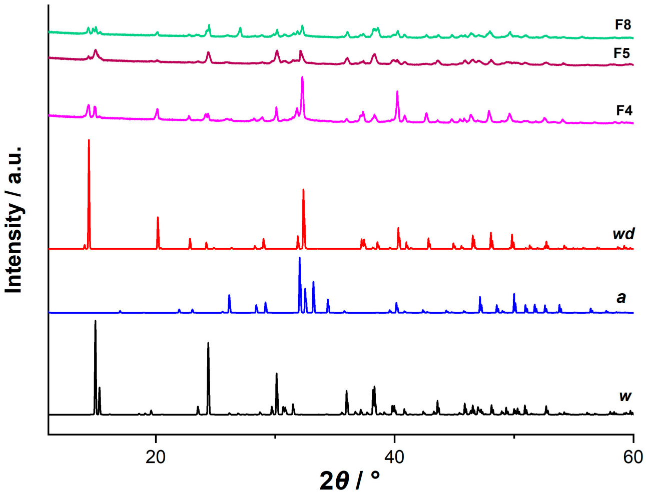

Figure 10. PXRD patterns of kidney stone samples F4, F5, and F8 compared to the data from the literature for whewellite (*w*), weddellite (*wd*), and hydroxyapatite (*a*) [40].

A thermogram of a typical sample in this group (F8) measured in the temperature range from 30 to 900 °C shows the mass loss in three steps (Figure 11): the first (100–250 °C) is water desorption, the second (350–500 °C) corresponds to the decomposition of anhydride oxalate and the release of CO, and the third, from 600 to 800 °C, corresponds to the decomposition of calcium carbonate. The remaining weight percent after heating is 49.0% [44] (the TGA/DSC findings for the remaining samples are presented in Supplementary Figure S3).

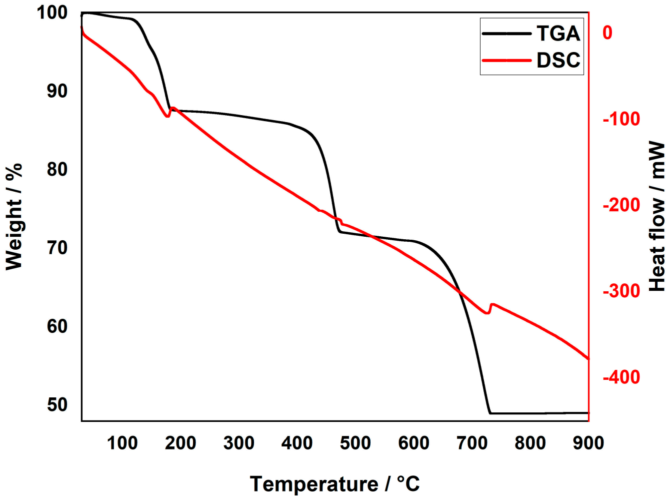

Figure 11. TGA and DSC curves for kidney stone sample F8 in an oxygen atmosphere.

Stereoscopic images of samples F4, F5, and F8, which belong to the group with a mixed calcium oxalate (*w* + *wd*) composition with some calcium phosphate (hydroxyapatite), are presented in Figure 12. The sizes of these kidney stones are as follows: F8: 6 × 4 mm; F4: 2.5 × 3 mm; and F5: 4 × 5 mm. Kidney stones that contain calcium oxalate (*w*, *wd*) but also other calcium phosphate minerals like hydroxyapatite have a characteristic morphology, with a rough, light to dark brown, heterogeneous coating that contains alternating whitish and brown layers [45].

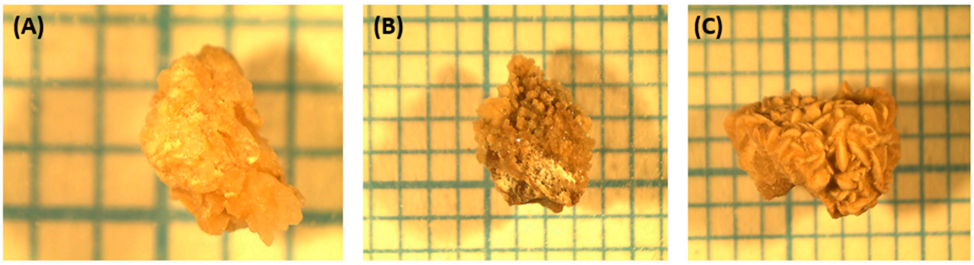

Figure 12. Stereoscopic microscope images of (**A**) F4, (**B**) F5, and (**C**) F8. Samples are placed on graph paper (1 × 1 mm).

The SEM microphotography in Figure 13 of the three samples of kidney stones F4, F5, and F8 shows their similar morphology. A significant amount of calcium oxalate (mostly whewellite) can be observed. For sample F4 in Figure 13A, a larger proportion of weddellite and phosphate, specifically hydroxyapatite, can be seen [46]. Kidney stone samples F5 and F8, shown in the SEM microphotography in Figure 13B,C, contain a higher proportion of whewellite, and this is clearly visible in the pictures. There are many small crystalline formations corresponding to whewellite, while sample F4 is smoother, which corresponds to an increased proportion of weddellite and apatite.

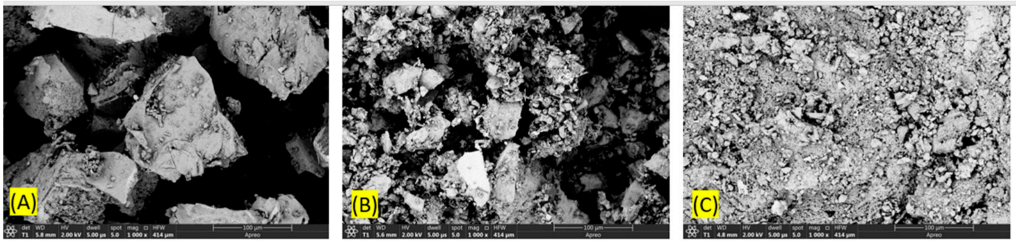

Figure 13. SEM images of (**A**) F4, (**B**) F5, and (**C**) F8. Magnification at 1000×.

The chemical (elemental) analysis of samples F4 and F5 (Figure 14A,B) shows that calcium (Ca), phosphorous (P), and oxygen (O) are the most present elements. This is expected because according to the other analyses, both samples are composed of mixed calcium oxalates (*w* and *wd*) and partly calcium phosphate. Comparing the EDX results for kidney stone samples F4 and F5, it is clearly visible that sample F4 contains a higher proportion of phosphate, which is consistent with the other results. As stated earlier (Figure 6, page 7), the presence of metallic trace elements may promote crystallization due to their ability to bind with the anions present in urine (oxalate, phosphate) [41]. In Figure 14A, it is visible that this stone sample contains several metals (Zn, Mg, and Al) that are in solution in the form of cations with a high charge density: +2 and +3 (EDX findings for sample F8 in Supplementary Figure S4).

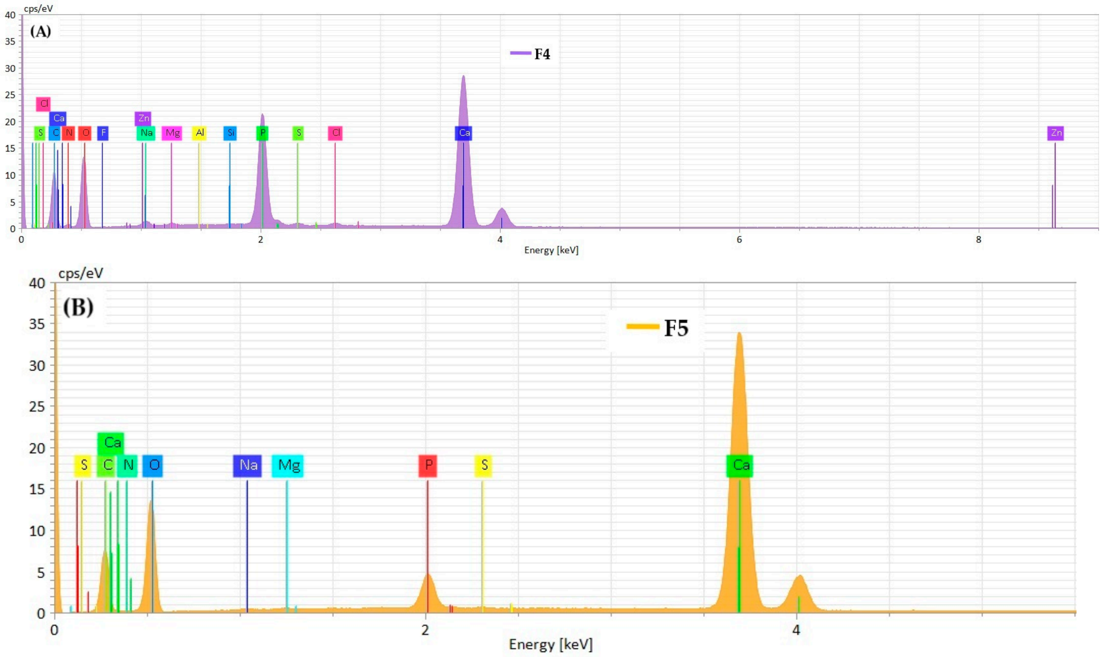

Figure 14. Elemental analysis (EDX) of samples (**A**) F4 and (**B**) F5. The peak height (cps/eV) represents the relative abundance of the elements detected in the samples.

The micro-CT cross-section of sample F8 in Figure 15 shows a higher amount of smaller whewellite crystals and clusters of rectangular weddellite crystals [32]. The small bright areas correspond to apatite, which is present mostly in the outer region of the cross-section.

3.1.2. Calcium Phosphate Kidney Stones (F1, F2, F3, M2, M4, and M7)

The IR spectra of all of the samples in the calcium phosphate group (Figure 16) show characteristic peaks at about 500, 1028, and 1500 cm^{-1} that correspond to the vibrations of the PO_4^{3-} group and a peak at about 3300 cm^{-1} from the OH^- group in water. According to the literature, a weak peak at about 600–630 cm^{-1} confirms that the phosphate is B-type francolite, in which the CO_3^{2-} groups are substituted with PO_4^{3-}. At about 572 cm^{-1}, a peak corresponding to the P-O bond vibration in the PO_4^{3-} group can be observed [47]. The IR spectra of the remaining two samples in this group (F2 and M2) are presented in Supplementary Figure S5.

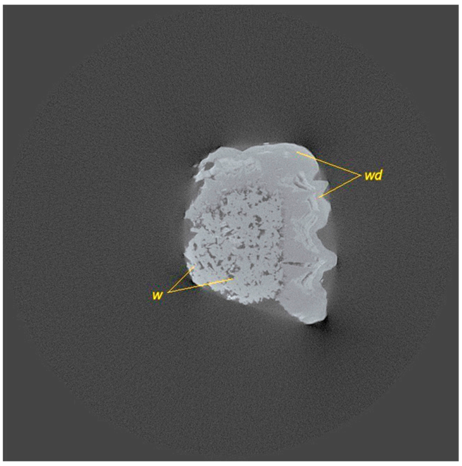

Figure 15. Micro-CT cross-section of kidney stone sample F8 (scan #511 out of the 1592 collected in total is presented).

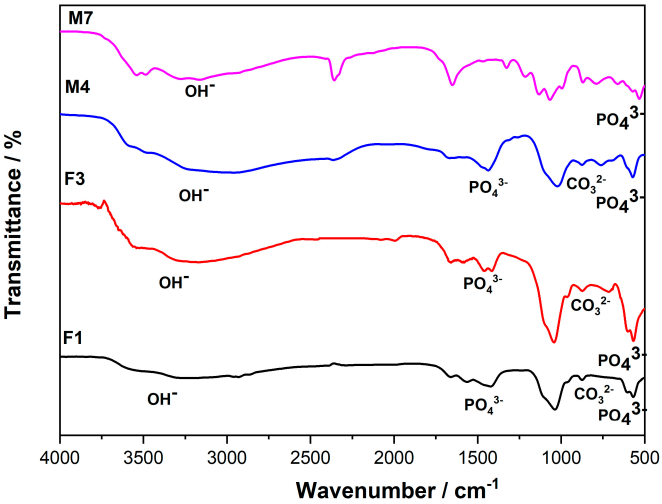

Figure 16. IR spectra of four samples of calcium phosphate kidney stones (F1, F3, M4, and M7). Data collected using DRIFT technique. Samples (5 mg) were mixed with spectroscopy-grade KBr (100 mg) before analysis. Characteristic bands are labeled at observed wavenumber.

The X-ray diffraction data (Figure 17) generally confirm the mineralogical composition of kidney stone samples F1, F3, M4, and M7. These samples are composed mostly of calcium phosphate (hydroxyapatite). Specifically, sample F1 contains 82%, F3 95%, and M7 51% hydroxyapatite. Sample M4 contains 51% struvite, and therefore, it predominantly consists of calcium ammonium phosphate, with a smaller amount of hydroxyapatite (37%). Another phosphate mineral, brushite (38%), is found together with apatite (51%) as a major component of sample M7. It also contains 10% weddellite. The powder X-ray diffractograms of the remaining two samples in this group (F2 and M2) are presented in Supplementary Figure S6.

The presence of weddellite was identified according to PDF card number 17-541. Struvite [48], hydroxyapatite [43], and brushite [49] were compared with the Crystallography Open Database (COD).

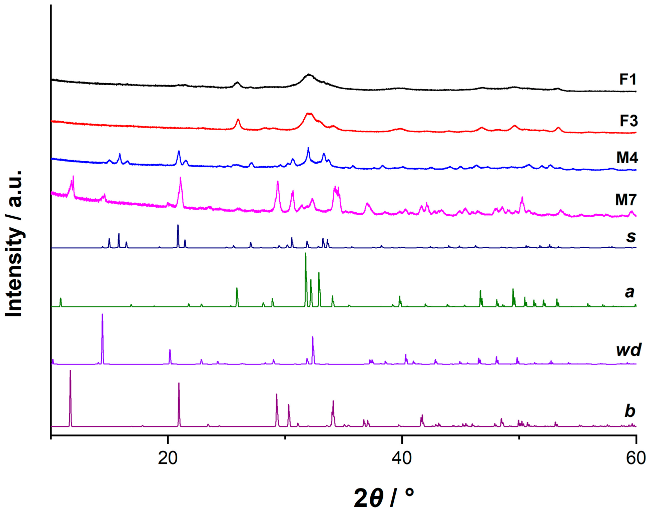

Figure 17. PXRD patterns of kidney stone samples F1, F3, M4, and M7 compared to standard data from the Powder Diffraction File (PDF) for weddellite (*wd*) and the Crystallography Open Database (COD) data for struvite (*s*), hydroxyapatite (*a*), and brushite (*b*).

As shown in Figure 18 for a typical sample in this group of kidney stones (F2—calcium phosphate), a remaining weight percent of 25% was recorded after heating. The first step at 30–250 °C is attributed to the desorption of water, and the second (600–850 °C) is attributed to the decomposition of the mineral carbonates that are present in the stones, together with phosphate, as indicated by FTIR (Figure 16) and PXRD (Figure 17). The thermograms of the other samples mentioned can be found in the Supplementary Materials (Figure S7) and also show similar results.

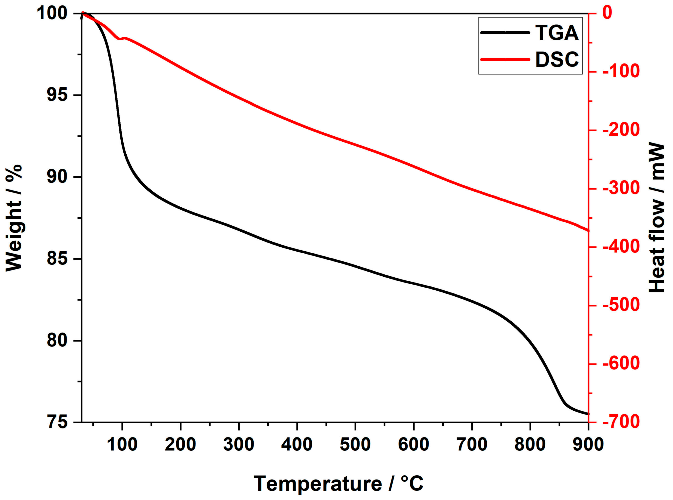

Figure 18. TGA and DSC curves for kidney stone sample F2 in an oxygen atmosphere.

Figure 19 shows stereoscopic microscope images of phosphate-type kidney stones F1 (6 × 5 mm), F2 (8 × 5.5 mm), F3 (6 × 4 mm), M2 (5 × 5 mm), M4 (3.5 × 5 mm), and M7 (6 × 5 mm). The stones presented in Figure 19, containing apatite (mostly sample F3) but also other phosphates, such as struvite (mostly sample M4) and brushite (M7), have a characteristic morphology, with a rough, light to dark brown, heterogeneous surface with alternating whitish and brown layers [50].

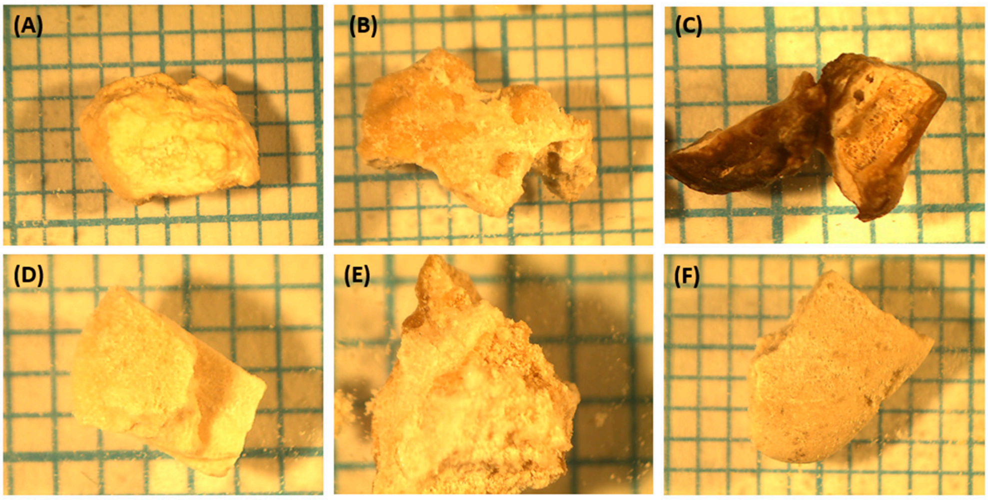

Figure 19. Stereoscopic microscope images of (**A**) F1, (**B**) F2, (**C**) F3, (**D**) M2, (**E**) M4, and (**F**) M7. Samples are placed on a graph paper (1 × 1 mm).

Phase identification and structural analysis of the kidney stones were carried out through thermal analysis (TGA/DSC, Figure 18), infrared spectroscopy, (FT-IR, Figure 16), and powder X-ray diffraction (PXRD, Figure 17). The results demonstrated that the primary solid phases identified in all of the systems investigated were phosphates: apatite, struvite, and/or brushite.

SEM microphotography of the six kidney stone samples in the phosphate group shows a uniform morphology, with apatite particles mostly of an irregular shape (Figure 20). Small granular crystals of *w* and often *wd*, together with larger phosphate crystals (magnesium ammonium phosphate–struvite), can be observed in Figure 20B,E.

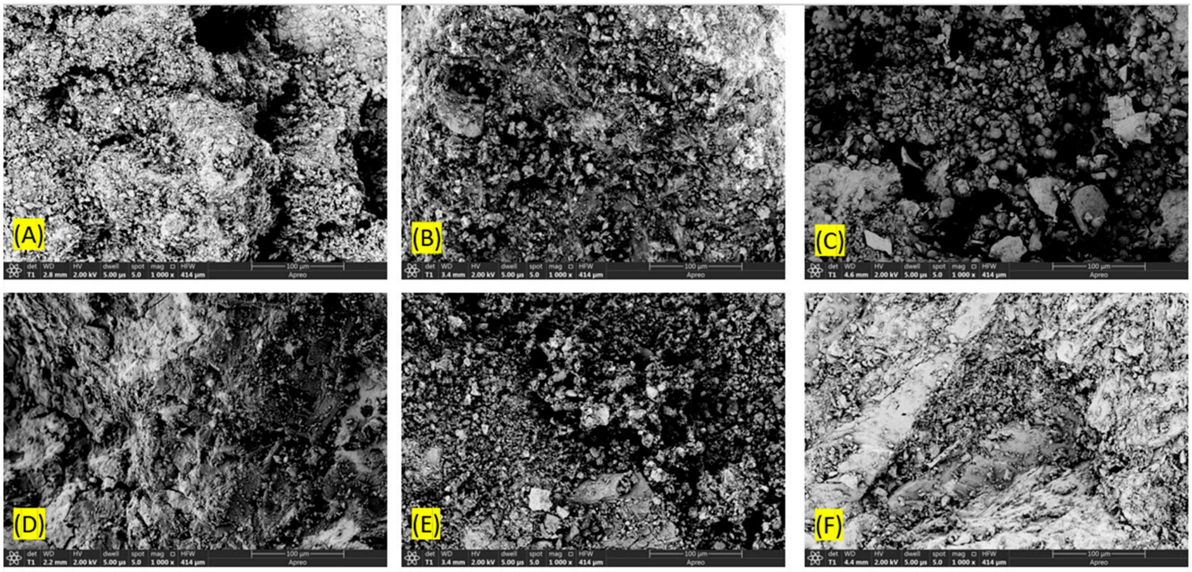

Figure 20. SEM microphotography of (**A**) F1, (**B**) F2, (**C**) F3, (**D**) M2, (**E**) M4, and (**F**) M7. Magnification at 1000×.

The chemical composition of samples F3 and M7 (Figure 21) with the highest content of calcium, phosphorous (apatite), and oxygen confirms the results of the IR and X-ray analyses that in all of the samples of this group (F1, F2, F3, M2, M4, and M7), the major mineral component is calcium phosphate, with a larger amount of apatite. For the other samples, the EDX results are shown in Supplementary Figure S8.

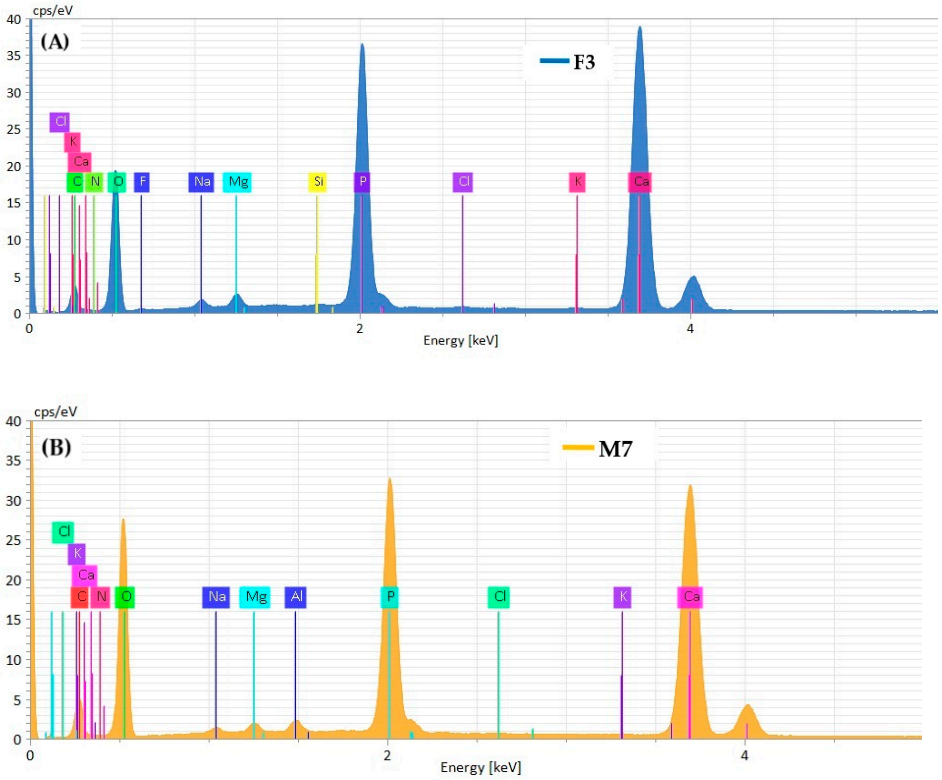

Figure 21. Elemental analysis (EDX) of samples (**A**) F3 and (**B**) M7. The peak height (cps/eV) represents the relative abundance of the elements detected in the samples.

The spatial distribution of the major elements (EDX mapping, Figure 22) in sample M7 shows their relatively uniform presence throughout the sample. The elemental analysis of sample M7 (Figure 21B) and the distribution map (Figure 22) show relatively high amounts and a uniform distribution of trace elements (specifically Mg and Na) [40].

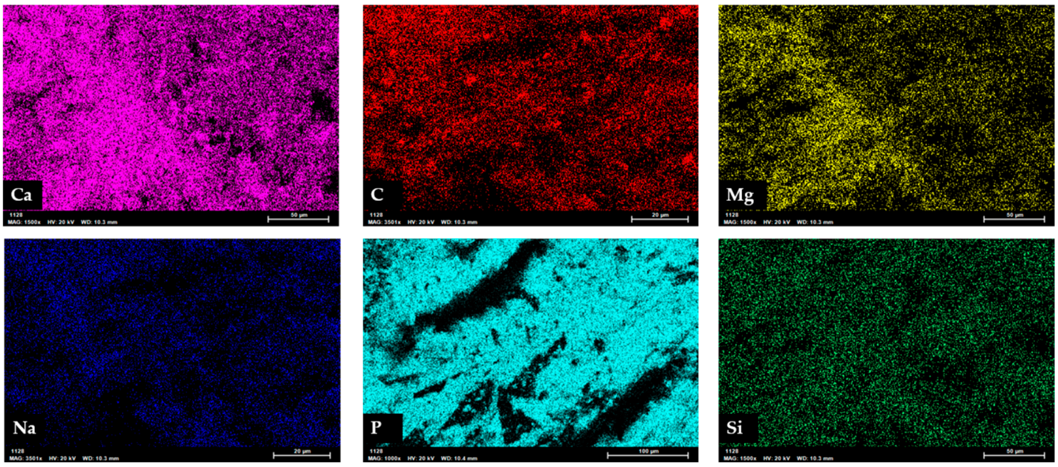

Figure 22. Elemental distribution map (EDX) of kidney stone sample M7. The intensity of color (brightness) represents the relative amount of a particular element in any given area.

The internal structure of the apatite kidney stone captured using micro-CT (Figure 23) shows typical concentric layers (with brighter and darker regions) [32]. Phosphorus, as the element with the highest atomic number, causes the highest X-ray attenuation. The uniform smaller regions in the stone's structure correspond to calcium oxalates.

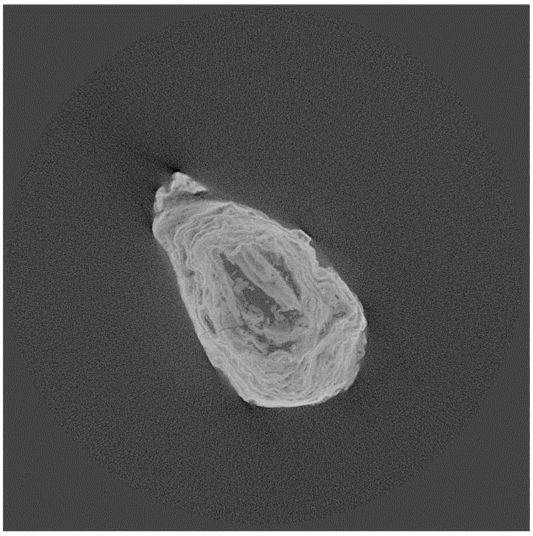

Figure 23. Micro-CT cross-section of apatite kidney stone sample F1(scan #879 out of the 1592 collected in total is presented).

As marked in Figure 24, micro-computed tomography shows the presence of apatite, which is the brightest area. The presence of a large portion of another phosphate mineral (38% of brushite) changes the interior structure significantly when compared to that in the previous micro-computed tomography findings (sample F1, Figure 23).

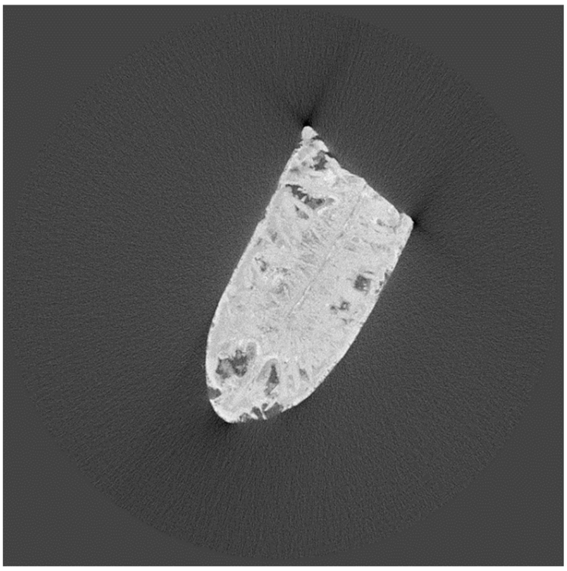

Figure 24. Micro-CT cross-section of kidney stone sample M7 (scan #939 out of the 1592 collected in total is presented).

3.2. Non-Calcium Stones (F7 and M8)

Samples F7 and M8 were categorized as non-calcium stones, as they contain other minerals in addition to calcium minerals, such as uric acid (F7) and cysteine (M8). Uric acid stones can be caused by a low pH value, a weakened ability to excrete uric acid, or the absence of certain known inhibitors (e.g., citrate). As the stones examined are heterogeneous in structure, it is very difficult to predict their formation without additional history, as stones that are heterogeneous reflect a more complex metabolic environment and often involve multiple risk factors [51–53].

Both infrared spectra in Figure 25 show a sharp peak at 1700 cm^{-1} corresponding to the C=O stretching in calcium oxalate monohydrate. Also, the bond vibrations in phosphate ions (PO_4^{3-}) at 900–1200 cm^{-1} and 300–600 cm^{-1} are present, as are peaks around 1027 and 1036 cm^{-1} corresponding to P–O stretching. Five sharp peaks at 1311, 1211, 1124, 1122, and 1027 cm^{-1} show the N–H stretching in the purine ring of uric acid. The evidence of the presence of uric acid is a band from C=O stretching at 1661 cm^{-1} [54].

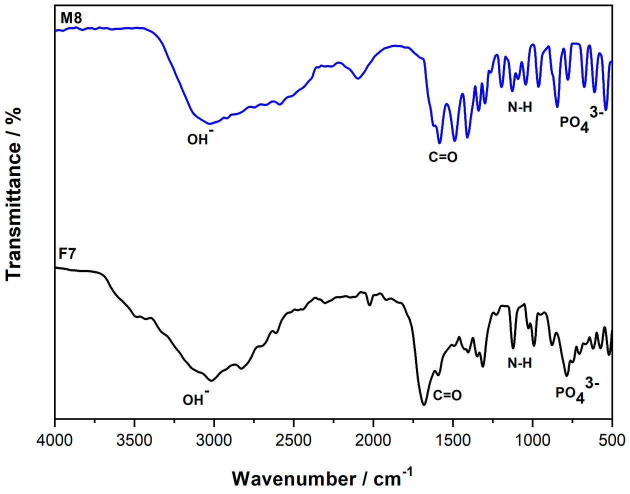

Figure 25. IR spectra of kidney stone samples F7 and M8. Data collected using DRIFT technique. Samples (5 mg) were mixed with spectroscopy-grade KBr (100 mg) before analysis. Characteristic bands are labeled at observed wavenumber.

Sample F7, as can be seen in Figure 26, correlates with the standards from the databases for uric acid [55] and whewellite. Sample M8 corresponds to cystine [56] and struvite [43].

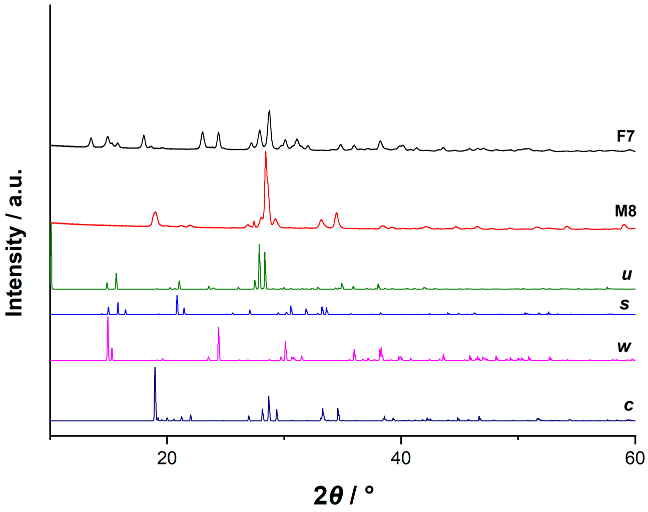

Figure 26. PXRD findings for two samples of kidney stones (M8 and F7) compared with data from the literature: uric acid (*u*) [50], whewellite (*w*), cystine (*c*) [51], and struvite (*s*) [43].

From the TGA/DSC graphs shown in Figure 27A, it can be seen that the mass loss occurs in three temperature ranges: 180–220 °C, 400–450 °C, and 580–650 °C. In the first step, water loss occurs; in the second, carbon monoxide is released; and in the third, carbon dioxide is released. The total weight percent loss is 34%. This shows that although this sample has a more complex composition, it still has a significant content of calcium oxalate. The thermal decomposition of kidney stone sample M8 shown in Figure 27B is observed to occur in one step [38], which confirms its major organic (cystine) component.

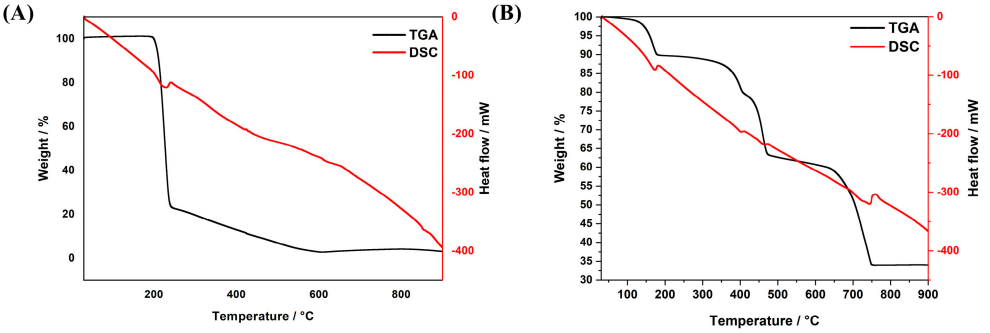

Figure 27. TGA (—) and DSC (—) curves for kidney stone samples F7 (**A**) and M8 (**B**) in an oxygen atmosphere.

Kidney stone sample F7 has an approximate size of 3.5 × 3.5 mm, and sample M8 is approximately 1.5 × 2 mm (Figure 28). Sample F7 appears as a pebble with a smooth but not polished surface. Sample M8 is colored similarly, but it is lighter. Stones that contain apatite but also other phosphates like struvite have a characteristic morphology, with a rough, light to dark brown, heterogeneous coating that contains alternating whitish and brown layers [45].

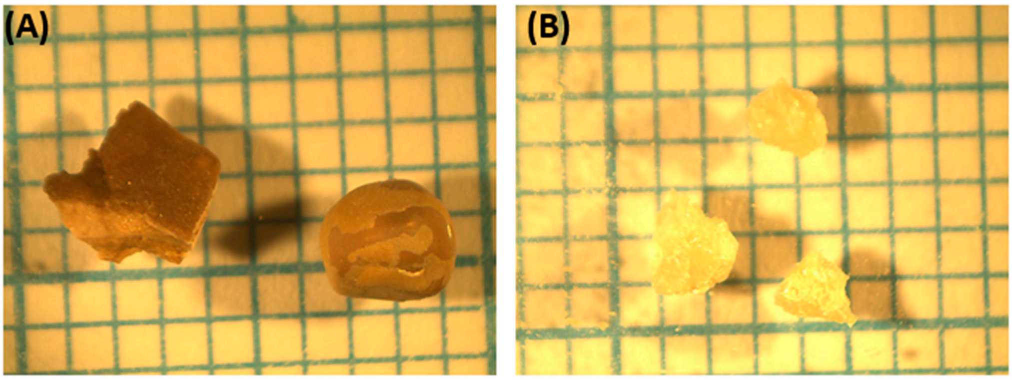

Figure 28. Stereoscopic microscope images of (**A**) F7 and (**B**) M8. Samples are placed on graph paper (1 × 1 mm).

The uric acid crystals appear mainly as agglomerates of platelet crystals with a heterogeneous matrix organization, while w is observed as small crystals. A granular appearance of the uric acid crystals and w crystals is observed (Figure 29A). Figure 29B represents kidney sample stone M8, which contains mostly cystine (82%) and phosphate, namely struvite (18%) [54].

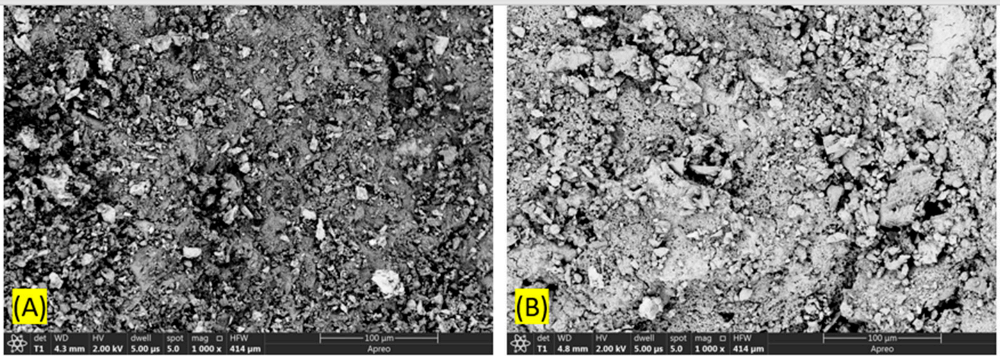

Figure 29. SEM microphotography of (**A**) F7 and (**B**) M8. Magnification at 1000×.

As expected for this kind of kidney stone (Figure 30) (M8, cystine + struvite), the most represented elements are C, O, and S, while the amount of Ca is much lower ("non-calcium stone"), and again, the presence of multivalent trace elements is observed (Fe, Al). The EDX results for sample F7 are presented in the Supplementary Materials (Figure S9).

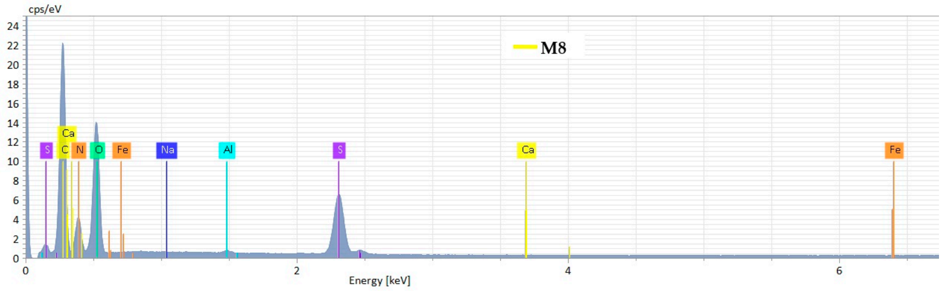

Figure 30. Elemental analysis (EDX) of sample M8. The peak height (cps/eV) represents the relative abundance of the elements detected in the sample.

4. Conclusions

Sixteen kidney stone samples, acquired using flexible ureterorenoscopy (FURS), were analyzed by means of chemical composition and structural/morphological characterization. Half of the samples were extracted from a female population and half from a male population of various origins. None of the kidney stone samples investigated consist of a pure chemical compound, as expected, and all of them contain at least a small amount of calcium oxalates (*w* and/or *wd*). In view of the fact that most of the stones analyzed are heterogeneous in nature, it is unfortunately not possible to draw a uniform conclusion, but each patient should be treated individually. Stones can be caused by various factors, such as diet, dehydration and certain metabolic disorders, but to find out the cause of the formation of each individual stone, in addition to a detailed morphological and quantitative analysis, other parameters, such as urine pH, urine volume, the presence of various ions in the urine, and dietary habits, must also be analyzed in detail. This research is particularly relevant given the rising prevalence of urolithiasis, especially in Western countries, where up to 15% of the population is affected. With this work, we aim to improve the understanding of the composition and formation of kidney stones to ultimately support the development of more effective treatments for this common and recurrent disease.

Supplementary Materials: The following supporting information can be downloaded at https://www.mdpi.com/article/10.3390/cryst15010006/s1. Table S1. Kidney stone samples with patient's year of birth, mineral composition, and Rietveld refinement parameters; Figure S1. TGA (—) and DSC (—) curves for kidney stone samples M5 and M6 in an oxygen atmosphere; Figure S2. Elemental analysis (EDX) of kidney stone samples (a) M1, (b) M5, (c) M6, and (d) F6. The peak height (cps/eV) represents the relative abundance of the elements detected in the sample; Figure S3. TGA (—) and DSC(—) curves for kidney stone samples F4 and F5 in an oxygen atmosphere; Figure S4. Elemental analysis (EDX) of kidney stone F8. The peak height (cps/eV) represents the relative abundance of the elements detected in the samples; Figure S5. IR spectra of two samples of calcium phosphate kidney stones, F2 and M2. Data collected using DRIFT technique. Samples (5 mg) were mixed with spectroscopy-grade KBr (100 mg) before analysis. Characteristic bands are labeled at observed wavenumber; Figure S6. PXRD patterns of two stone samples (F2 and M2) compared with data from the literature for weddellite (*wd*), struvite (*s*), and apatite (*a*) [45,50]; Figure S7. TGA (—) and DSC (—) curves for kidney stone samples F1 (a), M2 (b), and M7 (c) in an oxygen atmosphere; Figure S8. Elemental analysis (EDX) of kidney stone samples (a) F1, (b) F2, (c) M2, and (d) M4. The peak height (cps/eV) represents the relative abundance of the elements detected in the sample; Figure S9. Elemental analysis (EDX) of kidney stone sample F7. The peak height (cps/eV) represents the relative abundance of the elements detected in the sample.

Author Contributions: Conceptualization: J.B.K., A.S. and K.Ž.; methodology: J.B.K., K.Ž. and V.Š.; software: B.M., I.S. and Á.K.; validation: J.B.K., A.S. and N.M.M.; formal analysis: A.S.; investigation: J.B.K., K.Ž., V.Š. and A.S.; resources: V.Š. and A.S.; data curation: A.S.; writing—original draft preparation: J.B.K., K.Ž., B.M., N.M.M. and A.S.; writing—review and editing: A.S., N.M.M. and J.B.K.; visualization: I.S., Á.K. and J.B.K.; supervision: A.S.; project administration: A.S.; funding acquisition: A.S. and B.M. All authors have read and agreed to the published version of the manuscript.

Funding: This research was funded by PPUZN Stanković 2024/2027 (internal project of the Department of Chemistry at J.J. Strossmayer University of Osijek).

Data Availability Statement: The original contributions presented in this study are included in the article/Supplementary Material. Further inquiries can be directed to the corresponding author(s).

Conflicts of Interest: The authors declare no conflicts of interest.

References

1. Chen, I.H.; Yang, W.; Meyers, M.A. Alligator osteoderms: Mechanical behavior and hierarchical structure. *Mater. Sci. Eng. C Mater. Biol. Appl.* **2014**, *35*, 441–448. [CrossRef] [PubMed]
2. Morgan, E.F.; Unnikrisnan, G.U.; Hussein, A.I. Bone mechanical properties in healthy and diseased states. *Annu. Rev. Biomed. Eng.* **2018**, *20*, 119–143. [CrossRef] [PubMed]
3. Bertazzo, S.; Gentleman, E.; Cloyd, K.L.; Chester, A.H.; Yacoub, M.H.; Stevens, M.M. Nano-analytical electron microscopy reveals fundamental insights into human cardiovascular tissue calcification. *Nat. Mater.* **2013**, *12*, 576–583. [CrossRef] [PubMed]
4. Tan, A.C.; Pilgrim, M.G.; Fearn, S.; Bertazzo, S.; Tsolaki, E.; Morrell, A.P.; Nittala, M.G. Calcified nodules in retinal drusen are associated with disease progression in age-related macular degeneration. *Sci. Transl. Med.* **2018**, *10*, eaat4544. [CrossRef] [PubMed]
5. Durgawale, P.; Shariff, A.; Hendre, A.; Patil, S.; Sontakke, A. Chemical analysis of stones and its significance in urolithiasis. *Biomed. Res. India* **2010**, *21*, 305–310.
6. Radi, M.J. Calcium oxalate crystals in breast biopsies. An overlooked form of microcalcification associated with benign breast disease. *Arch. Pathol. Lab. Med.* **1989**, *113*, 1367–1369. [PubMed]
7. Aggarwal, K.P.; Narula, S.; Kakkar, M.; Tandon, C. Nephrolithiasis: Molecular mechanism of renal stone formation and the critical role played by modulators. *BioMed Res. Int.* **2013**, *2013*, 292953. [CrossRef]
8. Cox, R.F.; Hernandez-Santana, A.; Ramdass, S.; McMahon, G.; Harmey, J.H.; Morgan, M.P. Microcalcifications in breast cancer: Novel insights into the molecular mechanism and functional consequence of mammary mineralisation. *Br. J. Cancer* **2012**, *106*, 525–537. [CrossRef]
9. Morgan, M.P.; Cooke, M.M.; Christopherson, P.A.; Westfall, P.R.; McCarthy, G.M. Calcium hydroxyapatite promotes mitogenesis and matrix metalloproteinase expression in human breast cancer cell lines. *Mol. Carcinog.* **2001**, *32*, 111–117. [CrossRef] [PubMed]
10. Hutcheson, J.D.; Goettsch, C.; Bertazzo, S.; Maldonado, N.; Ruiz, J.L.; Goh, W.; Yabusaki, K.; Faits, T.; Bouten, C.; Franck, G.; et al. Genesis and growth of extracellular-vesicle-derived microcalcification in atherosclerotic plaques. *Nat. Mater.* **2016**, *15*, 335–343. [CrossRef] [PubMed]
11. Kapustin, A.N.; Chatrou, M.L.; Drozdov, I.; Zheng, Y.; Davidson, S.M.; Soong, D.; Furmanik, M.; Sanchis, P.; De Rosales, R.T.M.; Alvarez-Hernandez, D.; et al. Vascular smooth muscle cell calcification is mediated by regulated exosome secretion. *Circ. Res.* **2015**, *116*, 1312–1323. [CrossRef] [PubMed]
12. Baker, R.N.; Rogers, K.D.; Shepherd, N.; Stone, N. Analysis of breast tissue calcifications using FTIR spectroscopy. In *Diagnostic Optical Spectroscopy in Biomedicine IV, Proceedings of SPIE-OSA Biomedical Optics, Munich, Germany, 17–21 June 2007*; Optica Publishing Group: Washington, DC, USA, 2007; Volume 6628, p. 6628. [CrossRef]
13. Scales, C.D., Jr.; Tasian, G.E.; Schwaderer, A.L.; Goldfarb, D.S.; Star, R.A.; Kirkali, Z. Urinary stone disease: Advancing knowledge, patient care, and population health. *Clin. J. Am. Soc. Nephrol.* **2016**, *11*, 1305–1312. [CrossRef]
14. Xu, H.; Zisman, A.L.; Coe, F.L.; Worcester, E.M. Kidney stones: An update on current pharmacological management and future directions. *Expert. Opin. Pharmacother.* **2013**, *14*, 435–447. [CrossRef]
15. Taylor, E.N.; Stampfer, M.J.; Curhan, G.C. Obesity, weight gain, and the risk of kidney stones. *JAMA* **2005**, *293*, 455–462. [CrossRef] [PubMed]
16. Lieske, J.C.; De La Vega, L.S.P.; Gettman, M.T.; Slezak, J.M.; Bergstralh, E.J.; Melton, L.J.; Leibson, C.L. Diabetes mellitus and the risk of urinary tract stones: A population-based case-control study. *Am. J. Kidney Dis.* **2006**, *48*, 897–904. [CrossRef] [PubMed]
17. Taylor, E.N.; Stampfer, M.J.; Curhan, G.C. Diabetes mellitus and the risk of nephrolithiasis. *Kidney Int.* **2005**, *68*, 1230–1235. [CrossRef]

18. Alexander, R.T.; Hemmelgarn, B.R.; Wiebe, N.; Bello, A.; Samuel, S.; Klarenbach, S.W.; Curhan, G.C.; Tonelli, M. Kidney stones and cardiovascular events: A cohort study. *CJASN* **2014**, *9*, 506–512. [CrossRef]
19. Domingos, F.; Serra, A. Nephrolithiasis is associated with an increased prevalence of cardiovascular disease. *Nephrol. Dial. Transpl.* **2010**, *26*, 864–868. [CrossRef]
20. Alelign, T.; Petros, B. Kidney stone disease: An update on current concepts. *Adv. Urol.* **2018**, *2018*, 3068365. [CrossRef] [PubMed]
21. Ratkalkar, V.N.; Kleinman, J.G. Mechanisms of Stone Formation. *Clin. Rev. Bone Min. Metab.* **2011**, *3–4*, 187–197. [CrossRef] [PubMed]
22. Hess, B.; Hasler-Strub, U.; Ackermann, D.; Jaeger, P. Metabolic evaluation of patients with recurrent idiopathic calcium nephrolithiasis. *Nephrol. Dial. Transpl.* **1997**, *12*, 1362–1368. [CrossRef] [PubMed]
23. Cloutier, J.; Villa, L.; Traxer, O.; Daudon, M. Kidney stone analysis: "Give me your stone, I will tell you who you are!". *World J. Urol.* **2015**, *33*, 157–169. [CrossRef] [PubMed]
24. Reynolds, T.M. Chemical pathology clinical investigation and management of nephrolithiasis. *J. Clin. Pathol.* **2005**, *58*, 134–140. [CrossRef] [PubMed]
25. Khan, S.R.; Pearle, M.S.; Robertson, W.G.; Gambaro, G.; Canales, B.K.; Doizi, S.; Traxer, O.; Tiselius, H.G. Kidney stones. *Nat. Rev. Dis. Primers* **2016**, *2*, 16008. [CrossRef]
26. Moe, O.W. Kidney stones: Pathophysiology and medical management. *Lancet* **2006**, *367*, 333–344. [CrossRef]
27. Singh, P.; Enders, F.T.; Vaughan, L.E.; Bergstralh, E.J.; Knoedler, J.J.; Krambeck, A.E.; Lieske, J.C.; Rule, A.D. Stone composition among first-time symptomatic kidney stone formers in the community. *Mayo Clin. Proc.* **2015**, *90*, 1356–1365. [CrossRef] [PubMed]
28. Lieske, J.C.; Rule, A.D.; Krambeck, A.E.; Williams, J.C.; Bergstralh, E.J.; Mehta, R.A.; Moyer, T.P. Stone composition as a function of age and sex. *Clin. J. Am. Soc. Nephrol.* **2014**, *9*, 2141–2146. [CrossRef] [PubMed]
29. Ramona, P.; Bellanato, J.; Escolar, E. Infrared and Raman Spectroscopy of Urinary Calculi: A Rewiew. *Biospectroscopy* **1997**, *3*, 331–346. [CrossRef]
30. Cui, X.; Zhao, Z.; Zhang, G.; Chen, S.; Zhao, Y.; Lu, J. Analysis and classification of kidney stones based on Raman spectroscopy. *Biomed. Opt. Express* **2018**, *9*, 4175–4183. [CrossRef]
31. González-Enguita, C.; García-Giménez, R. Kidney Stones: Crystal Characterization. *Crystals* **2024**, *14*, 238. [CrossRef]
32. Williams, J.C.; Lingeman, J.E.; Daudon, M.; Bazin, D. Using micro computed tomographic imaging for analyzing kidney stones. *Comptes Rendus. Chim.* **2022**, *25*, 61–72. [CrossRef] [PubMed]
33. Robinson, J.W.; Roberts, W.W.; Matzger, A.J. Kidney stone growth through the lens of Raman mapping. *Sci. Rep.* **2024**, *14*, 10834. [CrossRef]
34. Tsujihata, M. Mechanism of calcium oxalate renal stone formation and renal tubular cell injury. *Int. J. Urol.* **2008**, *15*, 115–120. [CrossRef] [PubMed]
35. Gadd, G.M. Fungal Production of Citric and Oxalic Acid: Importance in Metal Speciation, Physiology and Biogeochemical Processes. *Adv. Microb. Physiol.* **2008**, *41*, 47–92. [CrossRef]
36. Izatulina, A.R.; Punin, Y.O.; Shtukenberg, A.G.; Frank-Kamenetskaya, O.V.; Gurzhiy, V.V. *Formation and Stability of Calcium Oxalates, the Main Crystalline Phases of Kidney Stones. Minerals as Advanced Materials II*; Springer: Berlin/Heidelberg, Germany, 2011; pp. 415–424. [CrossRef]
37. Pragnya, B.A.; Parimal, P. Analysis of urinary stone constituents using powder X-ray diffraction and FT–IR. *J. Chem. Sci.* **2008**, *120*, 267–273. [CrossRef]
38. Kaloustian, J.; El-Moselhy, F.; Portugal, H. Determination of calcium oxalate (mono- and dihydrate) in mixtures with magnesium ammonium phosphate or uric acid: The use of simultaneous thermal analysis in urinary calculi. *Clin. Chim. Acta* **2003**, *334*, 117–129. [CrossRef] [PubMed]
39. Daudon, M.; Bader, C.A.; Jungers, P. Urinary calculi: Review of classification methods and correlations with etiology. *Scanning Microsc.* **1993**, *7*, 1081–1106.
40. Manzoor, M.P.; Mujeeburahiman, M.; Rekha, P.D. Electron probe micro-analysis reveals the complexity of mineral deposition mechanisms in urinary stones. *Urolithiasis* **2019**, *47*, 137–148. [CrossRef]
41. Singh, V.K.; Rai, P.K. Kidney stone analysis techniques and the role of major and trace elements on their pathogenesis: A review. *Biophys. Rev.* **2014**, *6*, 291–310. [CrossRef]
42. Maruyama, M.; Sawada, K.P.; Tanaka, Y.; Okada, A.; Momma, K.; Nakamura, M.; Mori, R.; Furukawa, Y.; Sugiura, Y.; Tajiri, R.; et al. Quantitative analysis of calcium oxalate monohydrate and dihydrate for elucidating the formation mechanism of calcium oxalate kidney stones. *PLoS ONE* **2023**, *18*, e0282743. [CrossRef]
43. Veselinović, L.; Karanović, L.; Stojanović, Z.; Bračko, I.; Marković, S.; Ignjatović, N.; Uskoković, D. Crystal structure of cobalt-substituted calcium hydroxyapatite nanopowders prepared by hydrothermal processing. *J. Appl. Crystallogr.* **2010**, *43*, 320–327. [CrossRef]

44. Svoboda, R.; Zmrhalová, Z.O.; Galusek, D.; Brandová, D.; Chovanec, J. Thermal decomposition of mixed calcium oxalate hydrates—Kinetic deconvolution of complex heterogeneous processes. *Phys. Chem. Chem. Phys.* **2020**, *22*, 8889. [CrossRef] [PubMed]
45. Sekkoum, K.; Cheriti, A.; Taleb, S.; Belboukhari, N. FTIR spectroscopic study of human urinary stones from El Bayadh district (Algeria). *Arab. J. Chem.* **2011**, *9*, 3303334. [CrossRef]
46. Conti, C.; Brambilla, L.; Colombo, C.; Dellasega, D.; Gatta, G.D.; Realini, M.; Zerbi, G. Stability and transformation mechanism of weddellite nanocrystals studied by X-ray diffraction and infrared spectroscopy. *Phys. Chem. Chem. Phys.* **2010**, *12*, 14560–14566. [CrossRef]
47. Fleet, M.E. Infrared spectra of carbonate apatites: n2-Region bands. *Biomaterials* **2009**, *30*, 1473–1481. [CrossRef] [PubMed]
48. Ferraris, G.; Fuess, H.; Joswig, W. Neutron diffraction study of $MgNH_4PO_4*6H_2O$ (struvite) and survey of water molecules donating short hydrogen bonds. *Acta Crystallogr. Sect. B* **1986**, *42*, 253–258. [CrossRef]
49. Sainz-Diaz, C.I.; Villacampa, A.; Otalora, F. Crystallographic properties of the calcium phosphate mineral, brushite, by means of first principles calculations. *Am. Mineral.* **2004**, *89*, 307–313. [CrossRef]
50. Gavin, C.T.; Ali, S.N.; Tailly, T.; Olvera-Posada, D.; Alenezi, H.; Power, N.E.; Hou, J.; St Amant, A.H.; Luyt, L.G.; Wood, S.; et al. Novel Methods of Determining Urinary Calculi Composition: Petrographic Thin Sectioning of Calculi and Nanoscale Flow Cytometry Urinalysis. *Sci. Rep.* **2016**, *6*, 19328. [CrossRef] [PubMed]
51. Sakhaee, K.; Adams-Huet, B.; Moe, O.W.; Pak, C.Y.C. Pathophysiologic basis for normouricosuric uric acid nephrolithiasis. *Kidney Int.* **2002**, *62*, 971–979. [CrossRef]
52. Pak, C.Y.; Sakhaee, K.; Moe, O.; Preminger, G.M.; Poindexter, J.R.; Peterson, R.D.; Pietrow, P.; Ekeruo, W. Biochemical profile of stone-forming patients with diabetes mellitus. *Urology* **2003**, *61*, 523–527. [CrossRef]
53. Coe, F.L.; Parks, J.H.; Asplin, J.R. The pathogenesis and treatment of kidney stones. *N. Engl. J. Med.* **1992**, *327*, 1141–1152. [CrossRef]
54. Chandrajith, R.; Weerasingha, A.; Premaratne, K.M.; Gamage, D.; Abeygunasekera, A.M.; Joachimski, M.M.; Senaratne, A. Mineralogical, compositional and isotope characterization of human kidney stones (urolithiasis) in a Sri Lankan population. *Environ. Geochem. Health* **2019**, *41*, 1881–1894. [CrossRef]
55. Parkin, S.; Hope, H. Uric Acid Dihydrate Revisited. *Acta Crystallogr. Sect. B* **1998**, *54*, 339–344. [CrossRef]
56. Moggach, S.A.; Allan, D.R.; Parsons, S.; Sawyer, L.; Warren, J.E. The effect of pressure on the crystal structure of hexagonal L-cystine. *J. Synchrotron Radiat.* **2005**, *12*, 598–607. [CrossRef] [PubMed]

Disclaimer/Publisher's Note: The statements, opinions and data contained in all publications are solely those of the individual author(s) and contributor(s) and not of MDPI and/or the editor(s). MDPI and/or the editor(s) disclaim responsibility for any injury to people or property resulting from any ideas, methods, instructions or products referred to in the content.